# Anti-correlated Porosity–Permeability Changes During the Dissolution of Carbonate Rocks: Experimental Evidences and Modeling

**C. Garing · P. Gouze · M. Kassab · M. Riva · A. Guadagnini**

Received: 20 August 2014 / Accepted: 13 January 2015
Published online: 22 January 2015

C. Garing (✉) · P. Gouze · M. Kassab
Géosciences Montpellier, UMR 5243 CNRS/INSU, Université de Montpellier 2,
34095 Montpellier, France
e-mail: cgaring@stanford.edu

M. Kassab · M. Riva · A. Guadagnini
Dipartimento di Ingegneria Civile e Ambientale, Politecnico di Milano,
Piazza L. Da Vinci 32, 20133 Milano, Italy

M. Riva · A. Guadagnini
Department of Hydrology and Water Resources, University of Arizona,
Tucson, AZ 85721, USA

## Introduction

Carbonate rocks play a key role in geological, engineering and Earth science applications. They are ubiquitously found to host freshwater and/or hydrocarbon reserves and are frequently considered in the context of long-term $CO_2$ geological storage. These systems display a highly heterogeneous structure across a wide range of observation scales. The feedback of this multiscale heterogeneity on transport processes is still not completely documented and understood and poses significant challenges for predictive modeling (Fan et al. 2012; Saaltink et al. 2013). These potentially highly reactive environments are often flowed by aqueous solutions (such as meteoric water, seawater or hydrothermal water), which are not at equilibrium with the rock-forming minerals (Appelo and Postma 1993; Moore 2001; Noiriel et al. 2009; Luquot and Gouze 2009). Processes such as precipitation and/or dissolution can occur under these conditions and lead to complex dynamics altering the microstructural geo-metrical setting of the carbonate system. This ultimately affects the space-time distribution of key observable quantities such as porosity and permeability. For example, undersaturated conditions, often triggered by the acidification of the flowing fluid, lead to the dissolution of the rock-forming minerals (e.g., the carbonates and to a lesser extent the silicates), thus inducing porosity increase. This, in turn, can irreversibly affect the large-scale hydraulic behavior of the reservoir as driven by spatial variations of permeability and can markedly influence the distribution of solute concentrations and pathways. Detailed laboratory-scale investigation of these geochemical processes provides a critical contribution to document and understand the key features of the system dynamics and form the basis for the development of process-based models.

Experimental studies are notably challenging in the case of carbonate systems, due to the complex topological setting of the pore space (e.g., Siena et al. 2014 and references therein), which is often associated with low porosity values (Hebert et al. 2014 and references therein). A solid body of experimental evidences illustrates that the porosity increase resulting from carbonate dissolution is usually correlated with the increase of permeabil-ity. It is worth noticing that most of these experimental studies addressing the evolution of the pore space caused by carbonate dissolution involve highly reactive fluids, as the main field of application addresses the analysis of acidification techniques for enhancing near-well permeability (Cohen et al. 2008) and underground $CO_2$ storage (Luquot and Gouze 2009; Noiriel et al. 2009; Gouze and Luquot 2011; Hao et al. 2013; Smith et al. 2013; Wang et al. 2013; Tutolo et al. 2014). For instance, experiments such as those reported by Luquot and Gouze (2009) for limestones and Luhmann et al. (2014) for dolostones aimed at reproducing conditions occurring in the vicinity of a $CO_2$ injection well, where disequilibrium is maximal. These experiments suggest that there is generally a positive correlation between porosity and permeability changes and reveal that dissolution patterns may be quite different depending on the flow rate conditions and the degree of thermodynamic disequilibrium. The short residence time associated with locations close to the injection point triggers uniform dissolution because the effective dissolution rate is controlled by the surface kinetics and not by the renewing rate of the reactants and products, and the fluid tends to remain undersatu-rated over large distances. Heterogeneous dissolution patterns (manifesting in terms of, e.g., wormhole-like structures) may develop at intermediate to low flow rates (i.e., relatively long residence time) because of the initial and ever-increasing heterogeneity of the pore network

structure. As a general rule, the increase of permeability is triggered by an increase of the representative hydraulic radius of the pore-scale conduits, a decrease of the flow field tortuosity and, eventually, an increase of the connectivity of the percolating network (Gouze and Luquot 2011). However, the functional format of the relationship between porosity, $\phi$, and permeability, $k$, can be distinctly different depending on the initial pore space heterogeneity as well as prevailing hydrodynamic and chemical conditions.

A positive correlation between $\phi$ and $k$ associated with the overall increase of the size of the pores and throats that constitute the percolating pore network is not a rule in carbonate rocks. Few recent publications document a typical $\phi - k$ relationships with transient negative correlations (Mangane et al. 2013; Qajar et al. 2013; Luquot et al. 2014). Limestones are formed by the aggregation of grains spanning a large range of sizes and degrees of indura-tion and cementation among particles at the submicron level. Grains and cements in these geologically complex environments are characterized by distinctly diverse reactive surface areas and effective reaction rates. As a result, carbonate cements can be dissolved sometimes much faster than grains. Accordingly, one can speculate that solid particles can detach from the solid matrix and be transported by the moving fluid depending, e.g., on the degree of undersaturation of the reactive solution. Grains or particles detached from the matrix can migrate for some distances in the flow field without undergoing a complete dissolution in the presence of mildly undersaturated fluids. They can then settle in throat spaces and/or form dead ends where the possibility of dissolution to occur is limited by diffusion processes. These phenomena can cause a temporary or long-lasting decreasing trend of the medium perme-ability, depending on the feedback between the global increase of porosity and pore-throat clogging mechanisms. Indirect evidence of such detachment, transport and accumulation of particles was given by Mangane et al. (2013) who inferred the process of particles migra-tion and accumulation from an accurate evaluation of the mass distribution along the main flow path by relying on X-ray microtomography (XRMT). These authors concluded that the observed decrease of permeability associated with a porosity increase was due to the clog-ging of a fraction of the pore space of the macroporosity network by microporous material. Such clogging was triggered by the rearrangement of the detached undissolved particles, which eventually leads to the occurrence of low-permeability zones bridging the macrop-orosity areas and increasing the tortuosity while at the same time decreasing the sample-scale effective hydraulic radius.

The decrease of permeability (albeit with porosity increase) may have a critical impact on evolution of reservoirs. For example, it can result in a decrease of the reactivity of the flowing solution as residence time in the porous medium increases. In this context, environmental scenarios of interest include the occurrence of interactions between the carbonate matrix and fluid mixtures associated with relatively low reactivity. These conditions are typically repre-sentative of regions which are located at some distance from forcing boundaries and injection areas and might encompass significant portions of the host medium. A key aspect related to experiments mimicking these types of fields is to ensure the ability to monitor porosity and permeability evolution for relatively long time intervals to capture the relevant system dynamics. To the best of our knowledge, documentation of specific experiments targeting the system evolution under these conditions is still lacking. Here, we present experimen-tal evidence and interpretation of positive and anti-correlated dynamics of permeability and porosity in the context of dissolution experiments performed on cores of carbonate rocks. We investigate the way the rate of change of $\phi$ and $k$ and their correlation are controlled by the degree of undersaturation of the percolating solution for two different types of carbonate rocks. We do so upon employing deionized water (DW) and deionized water enriched with $CO_2$ (DW + $CO_2$). Deionized water is weakly undersaturated with respect to calcite, and

its degree of undersaturation increases when $CO_2$ is added. Both fluids may significantly dissolve the rock matrix within a time frame that is compatible with typical durations of laboratory-scale experiments. The use of DW instead of more multi-compositional water has the advantage of simplifying the chemical reactions taking place in the system and the pro-cedure for monitoring the solute concentrations. For two of the presented experiments, the microstructure of the pore space was investigated before and after dissolution has occurred by way of XRMT images. This allows documenting in details the changes of the medium at the microstructural level and identifying the occurrence of possible mechanisms of particle detachment and displacement.

The work is organized according to the following plan. Section 2 describes the experimen-tal setup and the characteristics of the rock samples investigated. The experimental results are detailed in Sect. 3, focusing first on the temporal evolution of permeability and poros-ity and then on the pore structure analysis. Finally, Sect. 4 presents a simple process-based model that is employed to interpret the alternating pattern in terms of positive and negative correlation between $\phi$ and $k$ observed when $CO_2$-enriched water or a less reactive fluid (DW) is flowed through the system.

## 2 Materials and Methods

In this section, we describe the key features of a set of experiments we performed to monitor porosity and permeability changes induced by the dissolution of two different types of car-bonate rocks in the presence of a percolating fluid, which is undersaturated with respect to calcite. As stated in Sect. 1, these conditions are considered to be representative of near sub-surface flow and transport scenarios or settings corresponding to deep injection of $CO_2$ and observations located at some distance from the forcing source. We adopted elementary geo-chemical conditions and alternated flow through the rock samples by employing a sequence of (a) deionized water equilibrated with atmosphere and (b) deionized water enriched with $CO_2$ to allow for simple and accurate mass balance assessment.

### 2.1 Experimental Setup and Protocol

We focus on experiments that are performed by injection of a percolating fluid at a constant flow rate, $Q = 10\ \mathrm{cm^3\ h^{-1}}$, through cylindrical cores of 9 mm diameter and 18 mm length of two types of carbonate rocks. Three experiments, hereafter termed M1, M2 and M3, are performed on core plugs which were sampled side-by-side in a reefal limestone from the Llucmajor platform (Mallorca, Spain). An additional experiment, termed L1, was performed on an oolitic limestone from the Lavoux (Paris Basin, France). These rock samples are characterized by distinctly different pore structures as detailed in Sect. 2.2.

Experiment M1 is performed by injecting deionized water at equilibrium with atmospheric pressure, i.e., containing $1.08 \times 10^{-5}\ \mathrm{mol\ L^{-1}}$ of $CO_2$ (pH of the inlet solution is $\mathrm{pH_{in}} = 5.5$), in the rock sample. Experiments M2, M3 and L1 are conducted by performing successive injections of (a) DW and (b) DW enriched with $3.62 \times 10^{-3}\ \mathrm{mol\ L^{-1}}$ of $CO_2$ (DW + $CO_2$). In this latter case, the inlet fluid is characterized by $\mathrm{pH_{in}} = 4.7$. Note that in the following, we use the term "cycle" to denote injection of DW followed by injection of DW + $CO_2$. Three cycles alternating DW and DW + $CO_2$ as injecting fluids are performed for M2, while M3 and L1 are, respectively, associated with one and two of such alternating cycles. The experimental conditions are listed in Table 1 together with the values of pH and calcium concentration expected at thermodynamic equilibrium with calcite, $\mathrm{pH_{eq}}$ and $[\mathrm{Ca}]_{\mathrm{eq}}$, respectively, for both

**Table 1** Experimental conditions (injected water, injection time, initial permeability $k_i$ and porosity $\phi_i$, pH of the injected water $pH_{in}$) and experimental results (final permeability $k_f$, porosity increase $\phi_f - \phi_i$, pH of the outlet $pH_{out}$ and mean calcium concentration in the outlet $<\Delta[Ca]>$)

| Injected water | Time (h) | $k_i$ (mD) | $k_f$ (mD) | $pH_{in}$ | $pH_{out}$ | $pH_{eq}$ | $<\Delta$[Ca]> (mg/L) | $\Delta[Ca]_{eq}$ (mg/L) | $\phi_i$ | $\phi_f - \phi_i$ |
|---|---|---|---|---|---|---|---|---|---|---|
| *M1* | | | | | | | | | | |
| DW | 0–**278** | 157.8 | 22.5 | 5.5 | 9.6 | 9.84 | 17 | 4.96 | 0.42 | 0.038 |
| *M2* | | | | | | | | | | |
| DW | 0–92 | 48.0 | 7.0 | 5.5 | 9.6 | 9.84 | 4.9 | 4.96 | | |
| DW + $CO_2$ | 92–193 | 7.0 | 36.5 | 4.62 | 6.7 | 6.97 | 35–45 | 99.7 | | |
| DW | 193–298 | 36.5 | 4.5 | 5.5 | 9.5 | 9.84 | 14–4.5 | 4.96 | 0.41 | 0.139 |
| DW + $CO_2$ | 298–430 | 4.5 | 10.6 | 4.65 | 6.7–6.6 | 6.97 | 36–46 | 99.7 | | |
| DW | 430–604 | 10.6 | 7.2 | 5.5 | 9.5 | 9.84 | 15–4 | 4.96 | | |
| DW + $CO_2$ | 604–**712** | 7.2 | 50.0 | 4.7 | 6.7–6.5 | 6.97 | 36–45 | 99.7 | | |
| *M3* | | | | | | | | | | |
| DW | 0–157 | 87.8 | 49.7 | 5.5 | 9.5 | 9.84 | 14 | 4.96 | 0.40 | 0.087 |
| DW + $CO_2$ | 157–**309** | 49.7 | 134.0 | 4.7 | 6.7–6.4 | 6.97 | 71 | 99.7 | | |
| *L1* | | | | | | | | | | |
| DW | 0–20 | 3.0 | 1.8 | 5.5 | 9.7 | 9.84 | 6 | 4.96 | | |
| DW + $CO_2$ | 20–162 | 3.27 | 8.2 | 4.8 | 7.6 | 6.97 | 38 | 99.7 | 0.25 | 0.085 |
| DW | 162–345 | 7.8 | 5.65 | 5.5 | 9.5 | 9.84 | 5 | 4.96 | | |
| DW + $CO_2$ | 345–**480** | 5.65 | 131.0 | 4.7 | 7.7–6.7 | 6.97 | 35 | 99.7 | | |

The values of pH, $pH_{eq}$, and calcium concentration, $\Delta[Ca]_{eq}$, at thermodynamic equilibrium with calcite are also listed
The time values in bold correspond to the total duration (final time) for each experiment, M1, M2, M3 and L1

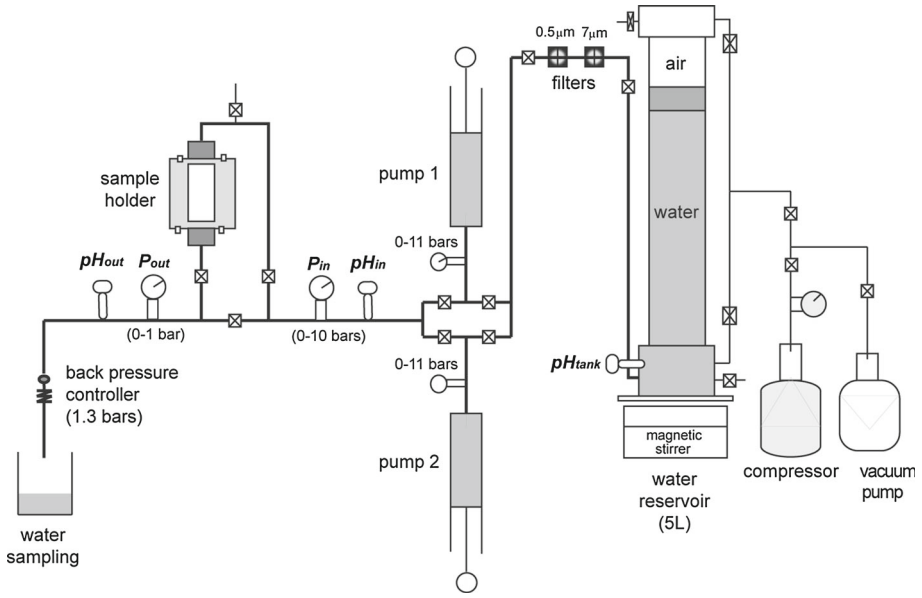


**Fig. 1** Diagram of the experimental setup

the DW and DW + $CO_2$ injected fluids. These values are obtained through the software PHREEQC (Parkhurst and Appelo 1999) and relying on its database.

Figure 1 depicts a sketch of the experimental rig setup for conducting our experiments. A motorized computer-controlled dual-piston pump system equipped with displacement encoders allows continuous injection of a given fluid flow rate into the sample. Feeding to the pumps is set by a cylindrical stirred reservoir equipped with a divider to isolate the fluid from the atmosphere and prepressurize it at 3.5 bars (0.35 MPa) before entering the pump. A pressure controller set at 1.3 bars (0.13 MPa) is installed at the outlet of the flow circuit to maintain a constant back pressure at the outlet of the sample. The rock sample cylinder is coated by a silicone sleeve and positioned into the percolation cell where a con-fining pressure is applied to force the flow through the sample. The flow circuit is equipped with three probes measuring the water pH in the reservoir ($pH_{tank}$), before the fluid enters the rock sample ($pH_{in}$)and at the sample outlet ($pH_{out}$). Two pressure gauges monitor pressure evolution at the inlet and outlet sections of the sample, respectively, written $P_{in}$ and $P_{out}$ in Fig. 1. The measure of $P_{out}$ allows checking the stability of the back-pressure controller.

The entire circuit (comprising the reservoir, pumps and tubing) is cleaned with a bactericide solution (composed of peracetic acid and hydrogen peroxide) before and after each experiment. It is then flushed with deionized water for at least two days and finally carefully vacuumed. The reservoir is then filled with the DW volume required for the subsequent experiment. The DW + $CO_2$ solution is prepared by adding the required $CO_2$ volume to the DW by means of a manual pump placed at the base of the reservoir. Subsequent injection cycles are performed by using two reservoirs and switching the circuit using valves following a procedure that avoids any mixing of the two water types within the pump. The sample is mounted inside the percolation cell and vacuumed before starting the experiment. The time evolution of the sample permeability, $k(t)$, $t$ being time, is calculated from the measured pressure drop, $\Delta P(t) = P_{in}(t) - P_{out}(t)$, and relying on Darcy's law

$$k(t) = -\frac{\mu L Q}{S \Delta P(t)}, \tag{1}$$

$\mu$ being fluid dynamic viscosity while $S$ and $L$ are the cross-sectional area and the length of the sample, respectively.

The outlet fluid is regularly sampled, and cation ($Ca^{2+}$ and $Mg^{2+}$) concentration is measured using a Varian Vista Pro CCD Simultaneous ICP-AES. For all experiments, the outlet $Mg^{2+}$ concentration is around 1 % of $Ca^{2+}$ concentration and is therefore considered to provide negligible contribution to mass balance. Accordingly, the dominant dissolution reaction occurring in the system is

$$CaCO_3 + H^+ \rightarrow Ca^{2+} + HCO_3^-. \tag{2}$$

Time-varying porosity, $\phi(t)$, is calculated from mass balance arguments considering measured calcium concentration as

$$\phi(t) = \phi_f - \frac{Q v_{CaCO_3}}{V} \int_t^{t_f} \Delta[Ca](\tau) d\tau. \tag{3}$$

Here, $\phi_f$ is the porosity of the sample at the end of the experiment, $V$ is the total volume of the
sample, $v_{CaCO_3}$ is the molar volume of calcite, and $\Delta[Ca] = [Ca]_{outlet} - [Ca]_{inlet} \equiv [Ca]_{outlet}$ because calcium concentration in the inlet water is below the detection limit.

## 2.2 Characterization of the Rock Samples

Ten cylindrical (9 mm diameter and 18 mm length) cores were extracted from selected rock samples from Mallorca and Lavoux. Porosity measurements were taken on a set of these cores using the triple weighting method on dry, saturated and immersed samples. Thin sections were extracted from an independent set of cores to provide detailed analyses of the rock structure and composition through optical microscopes and Environmental Scanning Electron Microscope (ESEM). In addition, some cores were scanned by three-dimensional XRMT using the ID19 beam line of the European Synchrotron Radiation facility (Grenoble, France) with a pixel size of 5.06 μm. For a single mineral rock (here calcite), the X-ray beam attenuation is proportional to the rock density, i.e., the porosity. Images are formed by voxels, which are coded in terms of gray levels. They are processed by way of ad-hoc algorithms described in Gouze et al. (2008) to estimate (a) the relative fraction of the solid, $\varphi_s$, and the voids defining macroporosity, $\varphi_m$ , i.e., pores with characteristic scale larger than the resolu-tion (5.06 μm), and (b) the microporous phase, $\varphi_\mu$, i.e., the voxels of rock containing pores of size smaller than the resolution. We also identified connectivity and topology of each phase together with location of interfaces between the phases following the methodologies detailed in Gouze et al. (2003), Noiriel et al. (2005) and Garing et al. (2014).

Figure 2 depicts XRMT images of cross sections of porous media samples (Fig. 2a for Mallorca and 2b for Lavoux) and selected ESEM ( Fig. 2c, e for Mallorca and 2d, f for Lavoux). In these figures, macropores appear in black and the gray level denotes the solid matrix density. Higher density (i.e., the massive carbonate) is in light gray. Medium gray values denote microporous matrix. The porosity of the microporous phase is given by the product of $\varphi_\mu$ and the mean intrinsic porosity of the phase, $\phi'_\mu$. The latter can be estimated from the gray level values of the XRMT images (Mangane et al. 2013; Garing et al. 2014). The porosity of the macroporous phase, $\phi_m$ , is equal to $\varphi_m$ . The total connected porosity of the sample is then $\phi_T = \phi_m + \varphi_\mu \phi'_\mu$, when the calculation of the different phase fraction is conducted on the clusters of (macro and micro) pores connecting the entire sample.

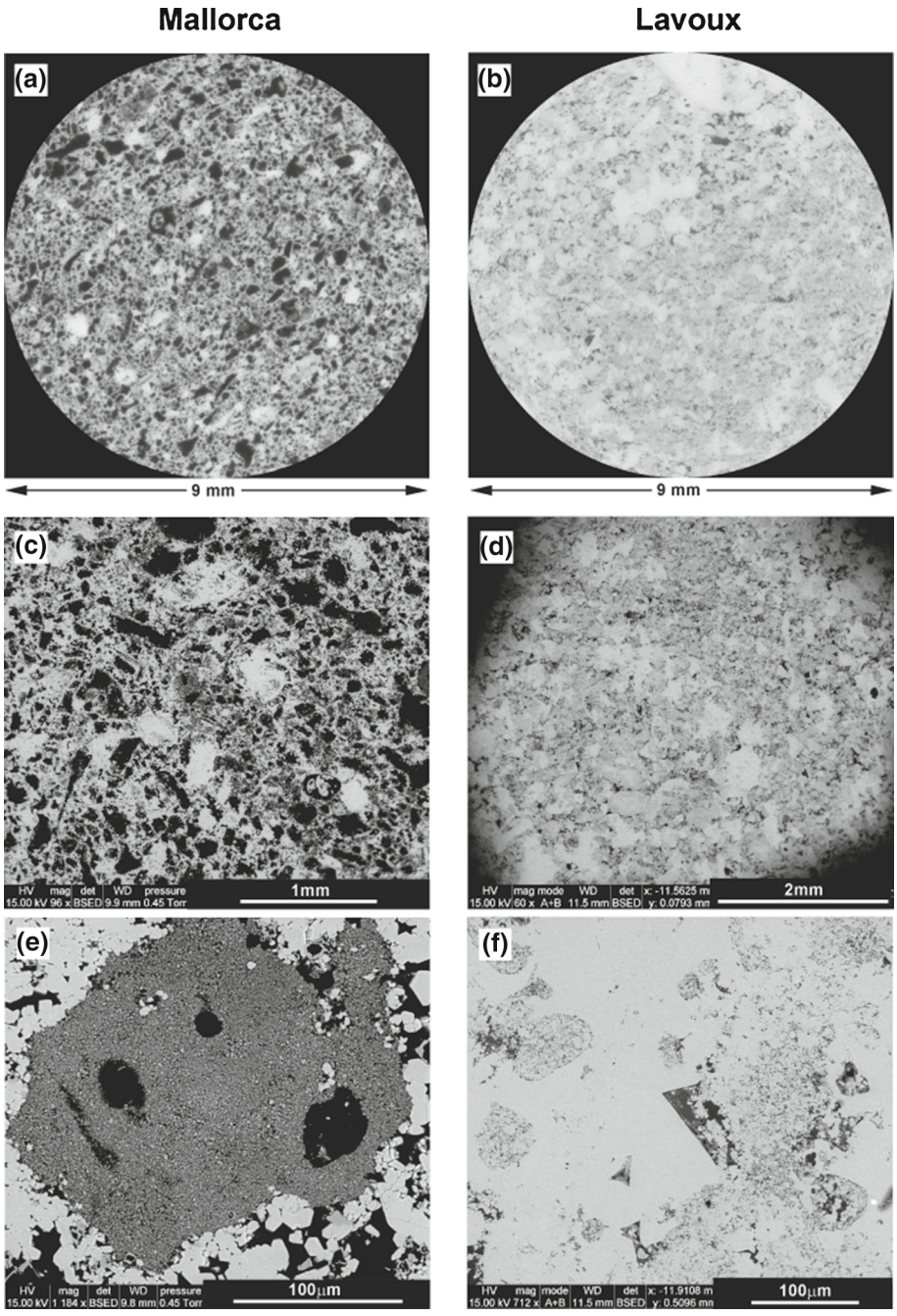


**Fig. 2** Examples of cross sections of Mallorca (**a**) and Lavoux (**b**) three-dimensional XRMT images and two-dimensional ESEM images at two different scales of Mallorca (**c**, **e**) and Lavoux (**d**, **f**) thin sections

The *Mallorca samples* were cored at a depth of 94 m within a borehole corresponding to the forereef unit of the Llucmajor Miocene reefal complex. The latter is formed by micritic bioclastic packstones and is the most homogeneous part of the carbonate platform (Garing 2011; Hebert 2011). Porosity measured in the laboratory on four cylinders cored side-by-side to the cores $M_1$, $M_2$ and $M_3$ (employed in experiments M1, M2, and M3, respectively) ranges from 0.39 to 0.44. Permeability was measured on four cylindrical samples (two of which are characterized by a 25 mm diameter and a 25 mm length and two by a 40 mm diameter and a 60 mm length) cored in the vicinity of $M_1$, $M_2$ and $M_3$. Measured permeabilities range between 30 and 180 mD, i.e., between $2.96\times10^{-14}$ and $1.78\times10^{-13}$ $m^2$. The analysis of thin sections by means of ESEM highlights that the Mallorca rock samples are very heterogeneous, displaying the occurrence of a calcite solid matrix associated with low-Mg content (<10 %of Mg), calcite micrograins associated with high-Mg content (60–80 % of Mg) and highly indurated pure calcite bioclasts (Fig. 2c, e). The microporous phase is composed of the Mg-rich carbonate grains of average size around 1 μm and of a microporous cement displaying the same composition of the solid matrix (calcite with low-Mg content). Close inspection and interpretation of these data allow anticipating that the microporous cement will be dissolved more easily than the dolomite grains because of the slower kinetics (Pokrovsky et al. 2009) and low reactive specific surface associated with the latter. With reference to Fig. 2a, one can note that the XRMT study of Mallorca samples also highlights the microscale heterogeneous nature of the rock type. Elaboration of data encapsulated in Fig. 2, and companion results (not shown) reveal that the average composition of the samples examined is: (i) macropores, with a relative volume fraction (or phase fraction) $0.10 \leq \varphi_m \leq 0.12$; (ii) micropore space, with a relative volume fraction $0.30 \leq \varphi_\mu \leq 0.35$; (iii) cements (i.e., the solid matrix phase without the indurated bioclasts), with a relative fraction $0.45 \leq \varphi_c \leq 0.48$; and (iv) indurated bioclasts, which constitute a volumetric fraction $0.05 \leq \varphi_b \leq 0.10$ of the sampled volumes. Note that the total volumetric fraction of the solid phase is $\varphi_s = \varphi_c + \varphi_b$. Macroporosity of all samples investigated is distributed over several unconnected clusters. Percolation in the Mallorca samples is mainly governed by the microporous phase that connects the macropore clusters. The microporous phase is highly porous ($\phi'_\mu$ around 91 %), and the total connected porosity $\phi_T$ computed for the imaged samples ranges from 0.40 to 0.44, depending on the samples.

The *Lavoux samples* were cored in a block extracted from a quarry located in the southwest of the Paris Basin, close to the city of Poitiers. This rock is a micritic grainstone with peloids, ooliths and bioclasts (Le Guen et al. 2007). Contrary to the Mallorca samples, the analysis shows that Lavoux carbonate is composed by pure calcite. Lavoux samples are less porous and permeable than Mallorca samples. The porosity measured on three 9-mm-diameter samples cored side-by-side to $L_1$ ranges between 0.246 and 0.256. Permeability measured on three cylindrical plugs (22.4 mm diameter and 45.6 mm length) by Le Guen et al. (2007) ranges between 7 and 14.1 mD, i.e., between $6.91 \times 10^{-15}$ and $1.39 \times 10^{-14}$ $m^2$. ESEM images show that the rock is composed of three phases: a solid matrix, macropores and microporous clusters (see, e.g., Fig. 2d, f). These three phases are also identified by the XRMT images (see Fig. 2b). This allows determining the following average composition of the *Lavoux* cores examined: (a) solid matrix ($\varphi_s = 0.55$); (b) macropores ($\varphi_m = 0.02$); and (c) microporous phase ($\varphi_\mu = 0.43$). Similarly to $M_1$ and $M_3$, the macropores are only connected by the microporous phase forming an overall connected network. Lavoux samples are less microporous than Mallorca samples with an intrinsic porosity of the microporous phase $\phi'_\mu = 0.54$, leading to a connected porosity $\phi_T = 0.25$ for the studied sample.

Statistical analysis of empirical density functions of pore sizes associated with macro-porosity related to the three-dimensional XRMT images has been performed upon relying

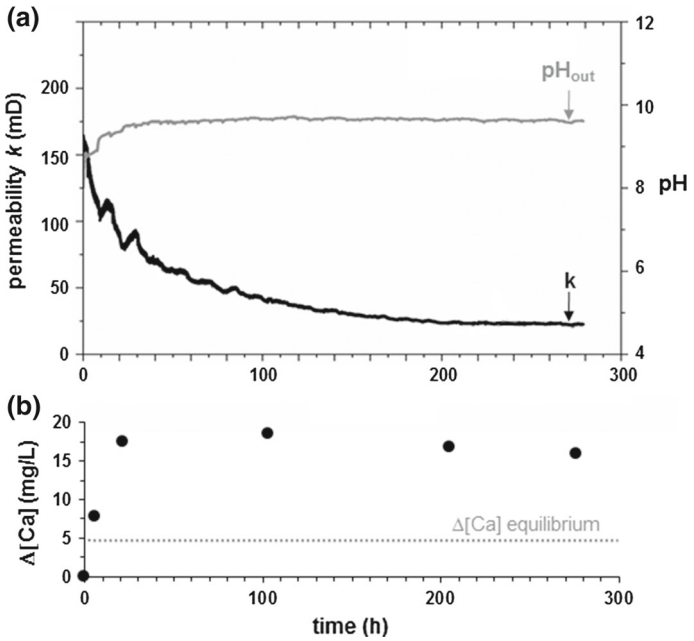


**Fig. 3** Temporal evolution of permeability, $k$, outlet pH, $pH_{out}$, (**a**) and $\Delta$[Ca] (**b**) during experiment M1; $\Delta$[Ca] at equilibrium (=$[Ca]_{eq}$) is also reported (*dashed curve*)

on a modified version of the algorithm described by Meijster et al. (2000). These results, as well as the statistical analysis of the average size of the macropores and micrograins of the two-dimensional ESEM images, show that the average pore size of the macropores in $L_1$ is much smaller (about 25 $\mu$m) than that associated with $M_1$ and $M_2$ (about 100 $\mu$m). This notwithstanding, the microporosity structure is similar for both rock types, with occurrence of pores associated with typical size less than 5 $\mu$m and very small (with size of about 1 $\mu$m) grains of calcite (for the Lavoux samples) or calcite and dolomite (for the Mallorca samples).

## 3 Experimental Results

Table 1 lists the complete set of quantitative results related to the dynamic evolution of the cores at the end of each injection cycle: the permeability ($k_f$), the outlet pH ($pH_{out}$), the mean calcium concentration measured in the outlet water ($< [Ca_{outlet}] >=< \Delta[Ca] >$) and the porosity increase $\phi_f - \phi_i$. Figure 3 depicts the temporal evolution of $pH_{out}$, $k$ and $\Delta[Ca]$ for experiment M1. Figs. 4, 5 and 6 depict analogous results obtained for experiments M2,
M3 and L1, respectively.

One can observe that permeability ubiquitously decreases or increases in the presence of percolating DW or $DW+CO_2$, respectively. The dynamics of permeability decrease detected during the first injection of DW are qualitatively similar for all experiments, displaying a power-law behavior with estimated slopes equal to $-0.78$, $-0.81$, $-0.61$ and $-0.26$ mD $h^{-1}$, respectively, for experiments M1, M2, M3 and L1. The decreasing and increasing trends observed for permeability during the subsequent DW injection phases for experiments M2 (Fig. 4) and L1 (Fig. 6) display slight discrepancies across the experiments, but are globally similar.

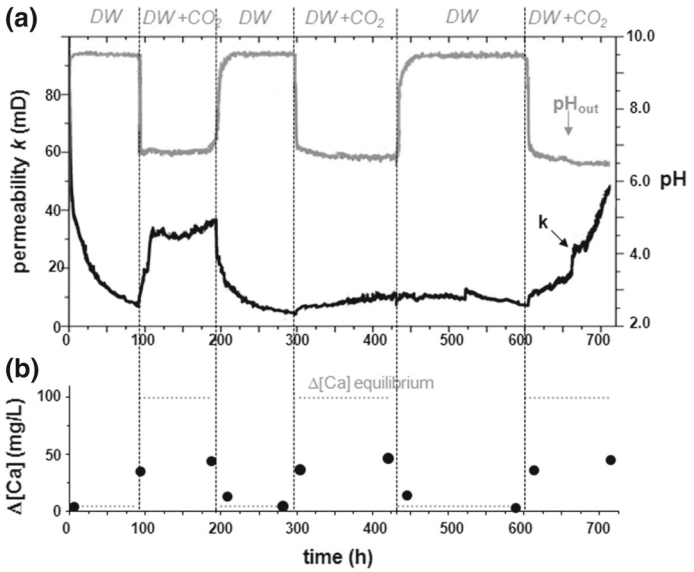


**Fig. 4** Temporal evolution of permeability, $k$, outlet pH, $pH_{out}$, (**a**) and $\Delta$[Ca] (**b**) during experiment M2; $\Delta$[Ca] at equilibrium (=$[Ca]_{eq}$) is also reported (*dashed curve*)

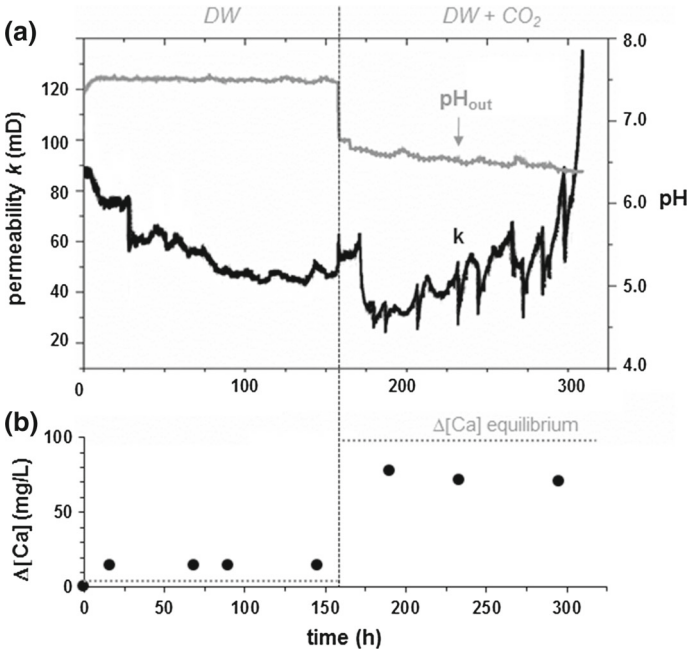


**Fig. 5** Temporal evolution of permeability, $k$, outlet pH, $pH_{out}$, (**a**) and $\Delta$[Ca] (**b**) during experiment M3; $\Delta$[Ca] at equilibrium (=$[Ca]_{eq}$) is also reported (*dashed curve*)

Positive values of $\Delta$[Ca] and ($pH_{out} - pH_{in}$) are measured for all of the experiments. These are associated with calcite dissolution and consequent porosity increase. Calcium concentration in the effluent water is almost constant during each cycle, suggesting that

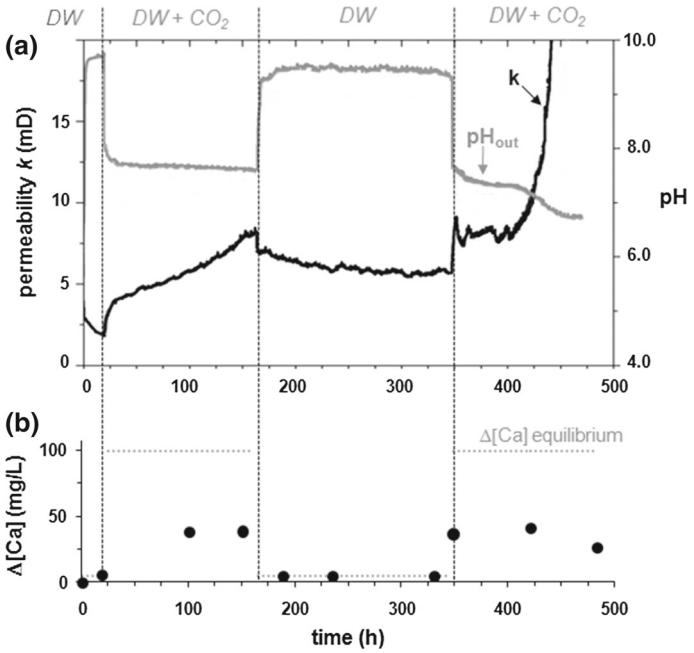


**Fig. 6** Temporal evolution of permeability, $k$, outlet pH, $pH_{out}$, (**a**) and $\Delta$[Ca] (**b**) during experiment L1; $\Delta$[Ca] at equilibrium (=$[Ca]_{eq}$) is also reported (*dashed curve*)

the effective kinetics at the scale of the core does not vary during the experiment. The large values of $\Delta$[Ca] observed during the DW + $CO_2$ injections are a consequence of the increased calcite dissolution associated with percolation of a fluid with increased reactivity. It is observed that the effluent Ca concentration is always close to or above the value expected at thermodynamical equilibrium ($\approx 5\,mg\,L^{-1}$) when DW is injected. As the Ca concentration is measured without any filtering and after acidification (that warrants the dissolution of all solid particles that could be present in the effluent fluid), values larger than that corresponding to equilibrium indicate the presence of calcite particles. Conversely, $\Delta$[Ca] is always lower than the equilibrium concentration $[Ca]_{eq}$ during DW + $CO_2$ injections. The change of Ca concentration clearly results from the kinetic-controlled dissolution taking place in the system, the effective kinetic rate being controlled by the disequilibrium state of the injected fluid.

The experiments are halted when the connected preferential paths break through the sample. For all experiments (with the exception of M1), the breakthrough occurs during a DW + $CO_2$ injection phase and is systematically associated with a fast increase of the permeability.

Specific behavior and relevant aspects of permeability and outlet $\Delta$[Ca] dynamics are detailed in the following for each experiment.

### 3.1 Experiment M1 (Mallorca, DW)

This experiment is characterized by a single injection of DW, for a total duration of 278 h (Table 1). Fig. 3a shows the occurrence of a permeability decreases until the end of the exper-

iment. Note that we repeated the same experiments (i.e., under the same experimental condi-tions) for five other Mallorca samples and observed trends similar to that depicted in Fig. 3a regardless the initial permeability of the samples, which ranged between 20 and 400 mD (i.e., between $1.97 \times 10^{-14}$ and $3.95 \times 10^{-13}$ $m^2$). Measured $\Delta$[Ca] is about 17 mg $L^{-1}$ (Fig. 3b), and mass balance shows that a volume of 45.1 $mm^3$ of calcite was dissolved or removed from the sample as flushed particles during the course of the experiment. This finding corresponds to a significant porosity increase of 3.8 %.

### 3.2 Experiment M2 (Mallorca, Three DW / DW + $CO_2$ Cycles)

This experiment is characterized by three cycles of alternating DW and DW + $CO_2$ injection, for a total duration of 712 h (Table 1).

Figure 4a shows that switching from DW to DW + $CO_2$ injection leads to a first sudden increase of permeability, which is then followed by a persistent increase associated with a slow rate. A subsequent power-law decrease of permeability is observed during the following DW injection. This is in turn followed by an increasing limb during the second injection of DW + $CO_2$. The rate of increase of permeability during this phase is much weaker than that observed during the first experimental cycle. The effect of the third injection of DW on permeability dynamics is relatively mild. This is likely due to the cumulative effect of the previous dissolution history where well-connected flow paths with large hydraulic radius have been created, thus markedly hampering the clogging effect of detached solid particles. After the last injection of DW + $CO_2$, the rock permeability significantly increases, almost reaching its initial value. The porosity increase rates, $\partial\phi/\partial t$, observed for the subsequent DW and DW + $CO_2$ phases are similar to those described above.

Stability of the chemical results depicted in Fig. 4b indicates that the dissolution rates are comparable during each cycle. These are (on average) 5 and 40 mg $L^{-1}$ during DW and DW+$CO_2$ injections, respectively. Accordingly, the different rates of change of permeability observed during the alternating injection phases can only be attributed to the changes of structural patterns of the pore network. The porosity of the tested rock core was increased by 13.9 % by the end of the experiment.

### 3.3 Experiment M3 (Mallorca, One DW / DW + $CO_2$ Cycle)

This experiment is characterized by a single cycle of alternating DW and DW+$CO_2$ injection, for a total duration of 309 h (Table 1).

Figure 5a indicates that the change in the chemical composition of the percolating water, which was imposed after 157 h from the beginning of experiment, starts to exert some influ-ence on permeability after a delay of roughly 20 h (corresponding to approximately 400 pore volumes). This indicates a strong memory effect of the pore structure inherited from the DW injection.

The subsequent increase of the permeability is highly irregular. This can be interpreted as the observed core-scale consequence of the concomitant dissolution and rearrangement of the solid particles in the pore network space. Particle clusters that accumulate during DW injection and clog some pore throats are partially dissolved during DW + $CO_2$ injection. A fraction of these particles may migrate in the system, being relocated until they eventu-ally accumulate in other throats along their path downstream. The large rate of increase of permeability observed at the end of the experiment (i.e., during the last 10 h) denotes the breakthrough of the preferential flow paths that are known to form in highly reactive systems (e.g., Kalia and Balakotaiah 2007; Luquot and Gouze 2009).

The measured values of $\Delta$[Ca] are around 14 and 71 mg/L, respectively, when DW or DW + $CO_2$ injection is performed (Fig. 5b). The slight decrease of both $\Delta$[Ca] and $pH_{out}$ observed at long times indicates a corresponding reduction of the effective dissolution rate, which can be tied to a general decrease of reactive surface area and is typically observed during the dissolution of carbonate due to highly reactive fluids (Luquot and Gouze 2009). Mass balance results show that the porosity has increased by 8.7 % at the end of the experiment.

### 3.4 Experiment L1 (Lavoux, Two DW / DW + $CO_2$ Cycles)

This experiment is characterized by two cycles of alternating DW and DW + $CO_2$ injection, for a total duration of 480 h (Table 1).

Figure 6a shows that the permeability decrease observed during the second DW injection occurs at a lower rate than during the first DW injection cycle. Permeability increases in a power-law fashion during the last DW + $CO_2$ injection, similar to what was observed in Fig. 5a with reference to M3. Figure 6 also reveals that measured values of $pH_{out}$ and $\Delta$[Ca] decrease during the last hours of the experiment, as observed in M3.

Similar to experiment M2 and in contrast with M3, switching boundary conditions in terms of injected fluid is followed by an immediate reverse of the temporal trend of the core-scale permeability. The relatively large difference observed during the injection of DW + $CO_2$ (Fig. 6b) between the effluent Ca concentration (around 35 mg/L) and the corresponding equilibrium value indicates that the effective dissolution rate is lower in the Lavoux sample than in Mallorca ones. This statement is supported by the observation that attaining the effective dissolution induced by DW + $CO_2$ injection requires significantly longer time for L1 than for M3. At the end of the experiment, the sample porosity was increased by 8.5 %.

## 4 Pore Structure Alteration

The detailed analysis of the pore space structure changes induced by the reactive fluid perco-lation is conducted (a) by ESEM on a thin section taken longitudinally from sample M2, and (b) by three-dimensional XRMT images of samples M1 and M3 acquired prior to and after the experiment (see also Sect. 2.2). The analysis of these XRMT images sup-ports our conceptual picture of the system behavior, which relies on the occurrence of the processes of (i) detachment of solid particles, (ii) their migration and (iii) subsequent deposition within pore throats, thus giving rise to anti-correlated porosity–permeability relationships.

The images taken at the end of the experiment are representative of the cumulative effects of DW and DW + $CO_2$ injections. The highest dissolution rate associated with the DW + $CO_2$ injection phase is expected to cause the removal of a large part of (a) the migrating solid particles and (b) the particle clusters which have eventually settled within pore throats. For these reasons, the dissolution pattern that is observed at the end of a given experiment is mostly controlled by the mass exchanges that occurred during the DW + $CO_2$ injection.

### 4.1 Single DW Injection (M1)

Figure 7 depicts two-dimensional ESEM images of two cross sections of the rock sample located at distances $z = 0.7$ and 4 mm from the inlet section. Fig. 7a, b refers to the top of the sample and highlights the occurrence of regions (marked as A in the figure) where dissolution is observed as well as areas (marked as B in the magnified subplot) associated

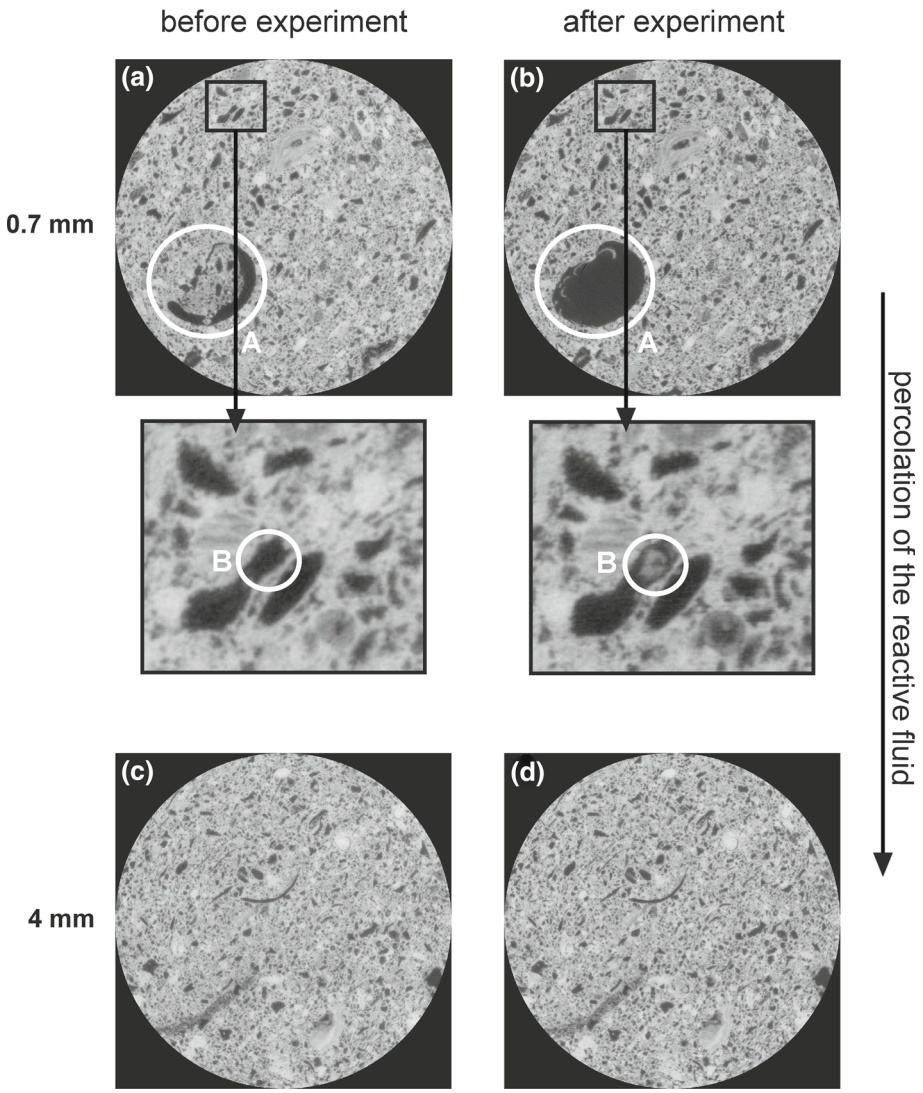


**Fig. 7** Example of XMRT cross sections at two different locations from the top of the sample prior to and after experiment M1. Water percolates the sample from the *top* to the *bottom*, as indicated by the *arrow* on the *right side*. Pixel size is 5.06 microns

with pores that are filled by solid particles during the experiment. The latter observation is consistent with a mechanism that is based on detachment of particles from the solid matrix and their subsequent migration in the flow field. At $z = 4$ mm, and throughout the remaining part of the sample, the images do not reveal significant changes of the pore structure. This is exemplified by Fig. 7c, d, depicting the ESEM images taken prior to and at the end of the experiment at the distance $z = 4$ mm from the top of core sample. These findings provide a strong indication that the injected fluid, DW, does not induce a high dissolution of the rock sample.

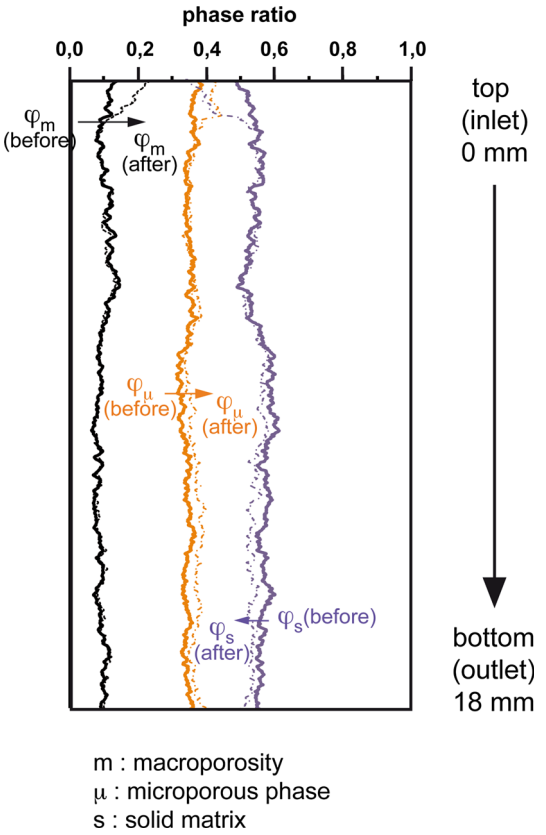


**Fig. 8** Phase fraction (ratio) of macroporosity ($\varphi_m$), microporous phase ($\varphi_\mu$) and solid matrix ($\varphi_s$) along the sample of 18 mm length from the *top* (*inlet*) to the *bottom* (*outlet*) before and after experiment M1 (*continuous* and *dotted curves*, respectively)

Figure 8 depicts the vertical distribution within the rock sample of the relative fractions of the diverse phases (macroporosity, microporous phase and solid matrix). The scenarios corresponding to the system states detected prior to and after experiment M1 are juxtaposed for ease of reference. These results support the observations stemming from the XRMT images and assist in describing phase transfer dynamics. Since the dissolution of the solid matrix is globally low during DW injection, the indurated bioclasts associated with the cement are not identified as a different phase, as we do below for sample M3. Macroporosity and microporosity at the very top of the sample show a distinct increase during the experiment because of dissolution of portions of the microporous phase and of the solid matrix. We then observe a slight decrease in macroporosity together with an increase in the fraction of solid matrix, which would correspond to the zone that contain most of the accumulated particles and therefore controls the permeability of the entire sample. Macroporosity at locations past this zone is only minimally affected by the percolation of the fluid. A slight increase of the microporous phase at the detriment of the solid matrix that is slightly dissolved is also observed at these locations, indicating that a fraction of the matrix volume is transformed into a microporous phase.

These results are summarized in Fig. 9a where the change of the profile of the solid fraction $\Delta\varphi_{\text{carb}} = (\varphi_\mu(1-\phi'_\mu)+\varphi_s)_{\text{after}} - (\varphi_\mu(1-\phi'_\mu)+\varphi_s)_{\text{before}}$ is reported. The average value of $\Delta\varphi_{\text{carb}}$ is negative, which denotes the bulk dissolution of the rock. However, positive values are locally observed, indicating the accumulation of solid particles. Results for sample M1 (Fig. 9, left panel) indicate particle accumulation in the vicinity of $z = 4$ mm.

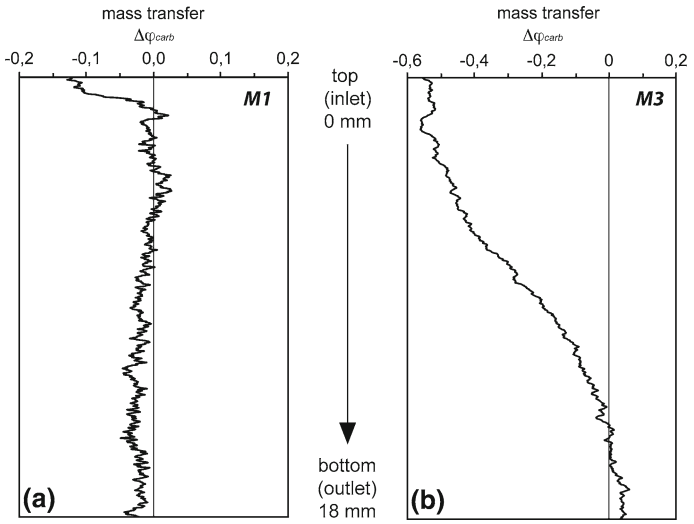


**Fig. 9** Change of the fraction of total solid (solid matrix and solid fraction of the microporous phase) between the end and the beginning of the experiment, $\Delta\varphi_{carb}$, along the sample of 18 mm length from the *top* (*inlet*) to the *bottom* (*outlet*), displayed for **a** experiment M1 and **b** experiment M3

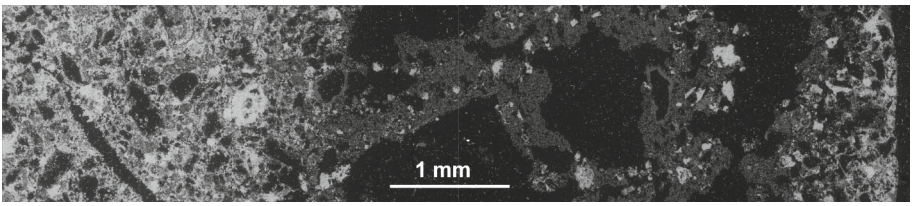


**Fig. 10** Example of ESEM images showing dissolution features at the end of experiment M2

## 4.2 DW and DW + $CO_2$ Injections (M2 and M3)

Figure 10 depicts a selected ESEM image corresponding to the top part of a thin section located at the core inlet and showing the dissolution features that are visible at the end of the experiment M2. The image shows that dissolution does not occur homogeneously inside the sample. This is likely due to the formation of preferential paths during the percolation of DW + $CO_2$. One can see that the most preserved part of the rock is located on the left part of the image. By comparison against Fig. 2c, one can note that the microstructure of the rock in this region is essentially unaltered at the end of the experiment. On the other hand, significant dissolution features are apparent in the right part of the image, where the percolation of the fluid has induced marked dissolution. In this latter region, it is observed that parts of the original solid material have been displaced and the size of the macropores is enhanced. The micrograins of dolomite (dark gray in Figs. 2cand 10) are still detectable in this zone. Calcite is preferentially dissolved, as expected from the kinetic difference, as calcite dissolution kinetics is ten times faster than dolomite dissolution (Pokrovsky et al. 2009). Some well-compacted microcrystalline calcite grains, corresponding to the indurated bioclasts fragments, also remain undissolved. Dissolution of these grains is difficult as compared to the microporous matrix so that the grains are likely to be transported by the fluid

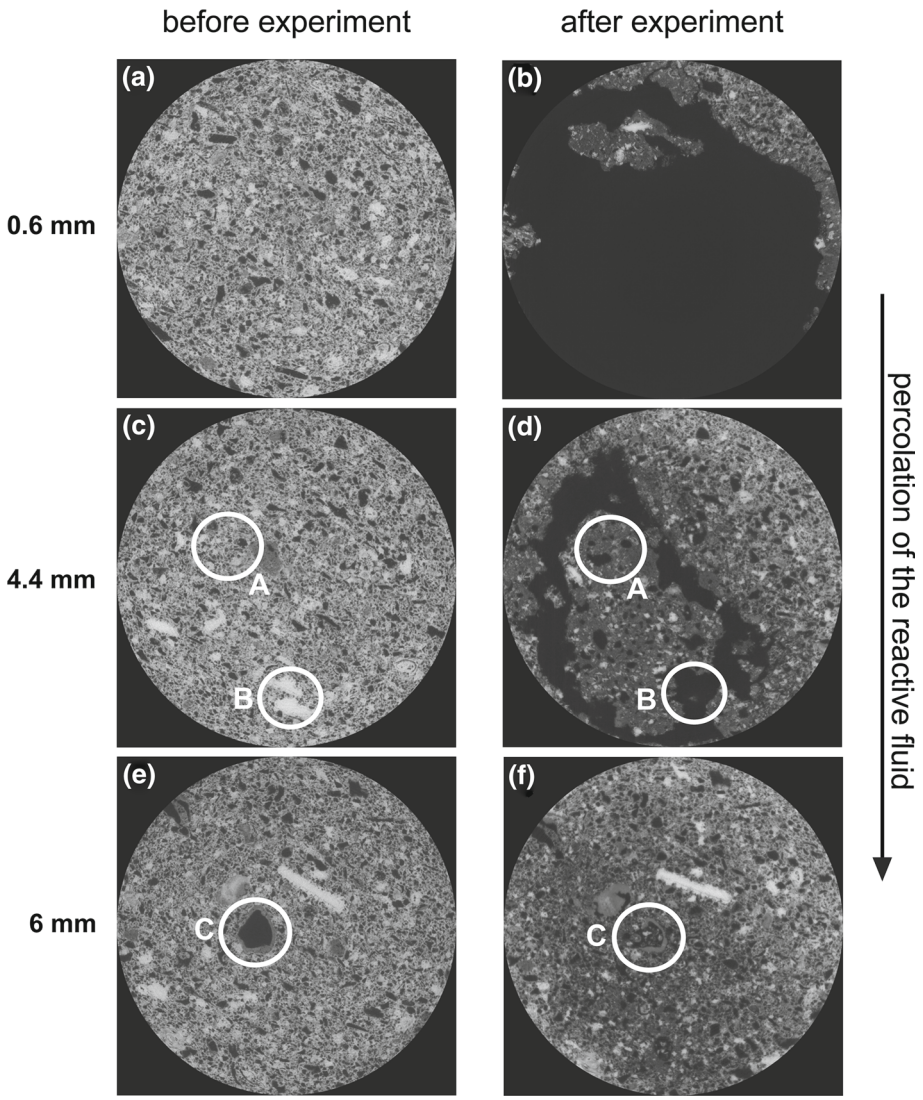


**Fig. 11** Example of XMRT cross sections at three different locations from the *top* to the *middle* of the sample prior to and after experiment M3. Water percolates the sample from the *top* to the *bottom*, as indicated by the *arrow* on the *right side*. Pixel size is 5.06 microns

while dissolution processes are still active and incomplete. A fine ESEM chemical analysis shows that the micrograins are formed by dolomite and calcite. Note that both dolomite and calcite particles are effectively detected in the system at the end of the experiment.

Similar to sample M1, the three-dimensional structure of sample M3 was investigated in details through XRMT imaging performed before and after the end of the experiment. Figure 11 depicts images of three cross sections of the rock core located at distances $z = 0.6$, 4.4 and 6.0 mm from the inlet section. It can be seen that the top region of the sample (Fig. 11a–d) has undergone high dissolution during the experiment while close to the middle section of

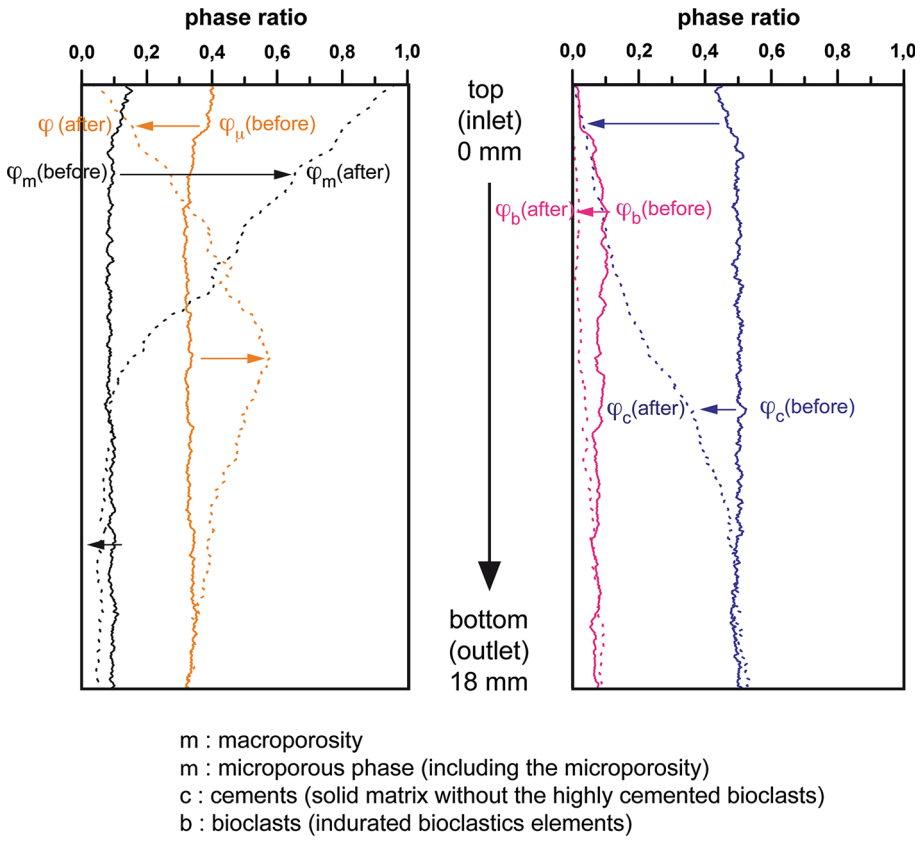


**Fig. 12** Phase fraction (ratio) of macroporosity ($\varphi_m$), microporous phase ($\varphi_\mu$), solid matrix separated into the cements ($\varphi_c$) and the indurated bioclasts ($\varphi_b$) along the sample of 18 mm length from the *top* (*inlet*) to the *bottom* (*outlet*) before and after experiment M3 (*continuous* and *dotted curves*, respectively)

the sample (Fig. 11e, f) dissolution is observed at a much lesser extent. At $z = 4.4$ mm, the matrix is not completely dissolved but is much more microporous. This feature is clearly seen by comparing the changes within the region marked as A in Fig. 11c, d. In some regions, e.g., zone B in Fig. 11c, d, some calcite indurated elements are not observed anymore at the end of the experiment. These elements are not likely to have been dissolved but rather detached from the cement and displaced in the macropores. We also note that the pores in region C in Fig. 11e, f are filled by solid particles during the experiment, as previously observed for experiment M1. Since most of the detached solid particles are dissolved during the DW + $CO_2$ injection stage, only a fraction of the particles mobilized during the DW phases might actually be observed by the end of the experiment.

Figure 12 depicts the vertical distribution within the block core of the relative fractions of the four identified phases (macroporosity, microporous phase, cements and indurated bioclasts). Macroporosity increases close to the inlet because of dissolution of the microporous phase and of the matrix (cement and few bioclasts), which is almost completely removed in the proximity to the inlet. We then observe a large microporosity increase at a distance of about 5–12 mm from the inlet while matrix dissolution still occurs. The solid mass transfer

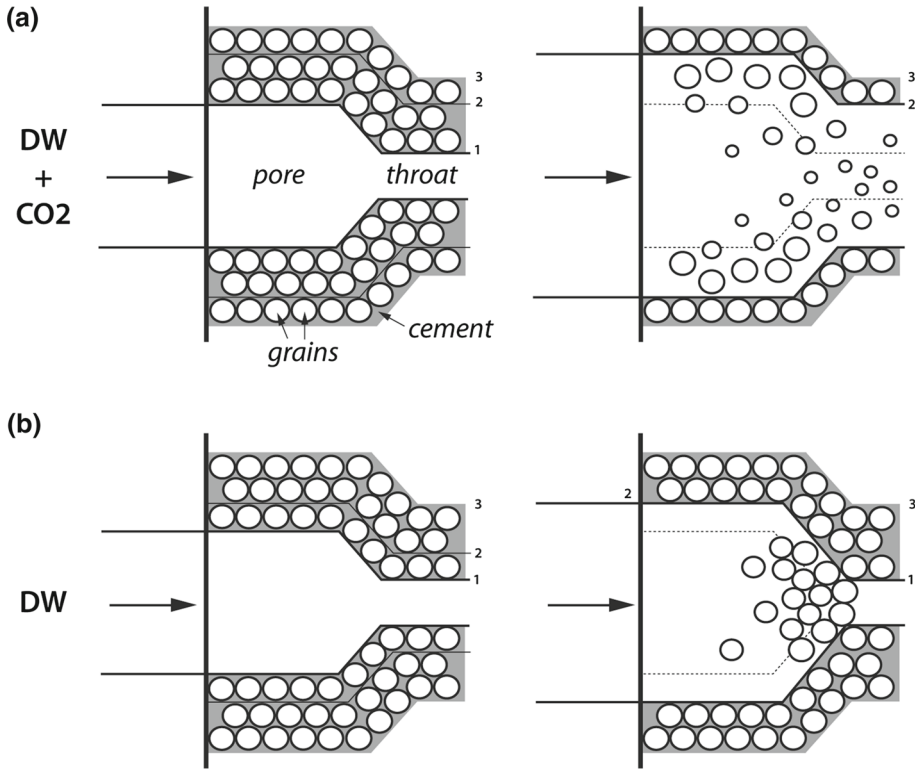


**Fig. 13** Graphical representation of the assumed mechanisms responsible for the observed $k - \phi$ trend during the injection of DW + $CO_2$ (**a**) and DW (**b**)

$\Delta\varphi_{\text{carb}}(z)$ profile is given in Fig. 9b and reveals an accumulation of solid particles at the bottom of the sample.

During injection of DW, the partial dissolution of the microporous phase and matrix close to the inlet favors detachment of solid particles. The latter tend to accumulate at locations downstream and form what we interpret as a microporous phase on the basis of XRMT imaging. Conversely, injection of DW + $CO_2$ hampers the formation of a microporous phase, in the sense that detached solid particles are dissolved before they reach pore clusters or existing microporous clusters. In addition, the microporous clusters are progressively and locally destroyed during this stage and preferential paths are formed.

## 5 Modeling

The mechanisms producing the observed porosity–permeability trends are schematically depicted in Fig. 13. The carbonate rock under consideration is formed by the aggregation of indurated grains and sparry calcite cement, the latter ensuring the cohesion of the matrix. Cements are dissolved faster than grains and then grains become free particles (Noiriel et al. 2009; Mangane et al. 2013).

When the rock is flowed by DW + $CO_2$, the cement is rapidly dissolved. As a consequence, the mobilized grains can be dissolved before they are dragged to an adjacent pore throat. The

increase of permeability is controlled by the increase of the effective hydraulic radius and the decrease of the tortuosity (Gouze and Luquot 2011). On these bases, we employ the power-law relationship proposed by Luquot and Gouze (2009) to model this type of evolution

$$k(t) = A\phi(t)^{\alpha} \tag{4}$$

where $\phi(t)$ is given by (3) while $A$ [$L^2$] and $\alpha$ [.] are model parameters that can be estimated on the basis of experimental data. Albeit having been initially established in the context of percolation theory (Sahimi 1994), the use of a power-law model to describe macroscopically these types of processes taking place in complex pore spaces typical of natural rocks is also grounded on experimental observations (e.g., Smith et al. 2013; Luhmann et al. 2014). As such, we should consider the predictive ability of this type of semiempirical model solely within the range of permeability scanned through the experimental conditions, also noticing that permeability changes are rarely seen to range over several orders of magnitude within a given experiment. The estimate of the exponent $\alpha$ is controlled by both the heterogeneity (pore structure) of the rock and the dissolution regime. The latter is usually characterized by the Peclet (*Pe*) and Damköhler (*Da*) numbers, which provide an appraisal of the relative strengths of the characteristic time of the mass transfer by diffusion, advection and reaction (Golfier et al. 2002; Gouze and Luquot 2011). Accordingly, the value of $\alpha$ is expected to change during dissolution due to (a) modifications of the pore network geometry, and (b) changes of *Pe* and *Da*. For instance, the increase of porosity during dissolution will contribute to decrease the value of *Pe*, while the formation of preferential flow path will cause the effective reactive surface area and therefore the value of *Da* to decrease.

When DW is pumped through the rock sample, the dissolution rate of both cement and grains is lower than that observed when $CO_2$ is added to the DW. Therefore, we conjecture that the time required for the complete dissolution of the free grains is longer than that required for the grains to reach the next pore throat. The ensuing accumulation of the grains is then in competition with local dissolution processes and can trigger the decrease of permeability by increasing head losses in the vicinity of the pore throats (see Fig. 13). On these bases, one can assume that the observed monotonic decrease of the core-scale permeability is predominantly controlled through the clogging of the throats by the detached particles. The rate at which the permeability decreases depends mainly on (1) the initial value of the pore-throat average diameter that controls the beginning of the accumulation of the grains, and (2) the rate of particle detachment, which depends on the pore–fluid interface area.

The different rates of permeability decrease observed for each injection of DW suggest that the dominant process that controls the permeability change is the effect of the increase of the mass and volume of the cluster of detached particles relative to the initial average size of the throats. Detailed exploration of the physics governing the competition between (a) the dissolution of detached particles of various sizes during their migration in the system, and (b) the accumulation of such particles in the heterogeneous void space is far beyond the scope of this paper. Here, we focus on the development and parameterization of a simple heuristic model that may be used to interpret our experimental observations. To account for the anti-correlated porosity–permeability changes during injection of deionized water, we propose to model the time evolution of permeability by an exponential expression that encapsulates the effect of the accumulation of the particles on the dynamics of $k$:

$$k(t) = B\exp(-\beta t) \tag{5}$$

Here, $B$ [$L^2$] and $\beta$ [$T^{-1}$] are parameters that are estimated on the basis of the experimental data. We note that exponential temporal decreases of permeability have been often documented when a tight porous medium is subject to mechanical constraints. Exponential

decrease of porosity and permeability triggered by compaction was first described by Athy's model (Athy 1930) and then discussed in numerous publications (e.g., Schneider et al. 1996; Rutqvist and Stephansson 2003). Whereas these mechanisms are different from those occurring in our experiments, one can argue that the accumulation of particles at the throat inlet acts as a common element which increases head losses in both cases.

The scaling coefficients $A$ and $B$ are invariant during the dissolution stage and can be related to the initial bulk properties of the pore network. As such, the proposed phenomenological model can be relevant and may have some predictive power in the presence of relatively small changes in porosity. This issue was also discussed in Luquot and Gouze (2009) with reference to (4). The exponents $\alpha$ and $\beta$ imbue the characterization of dominance between the competitive dissolution and accumulation regimes associated with each of the DW + $CO_2$ and DW stages. We emphasize that detailed testing the predictive power of such simple models in the settings here considered hinges on the exploration of the proper physical meaning of the model structure and parameters. This would require, e.g., detailed and rigorous theoretical investigation about the way the effect of pore-scale processes can be transferred to macroscale relationships of the kind presented in (4) or (5), which is outside the scope of this contribution.

Modeling results for the time evolution of permeability based on (4), (5)and fittedtothe data by least squares are depicted in Fig. 14 together with their associated 95 % confidence intervals. The experimental $k$ data and porosity values determined from the chemical analysis through (3) are also depicted. Parameters of (4) are estimated on the basis of data associated

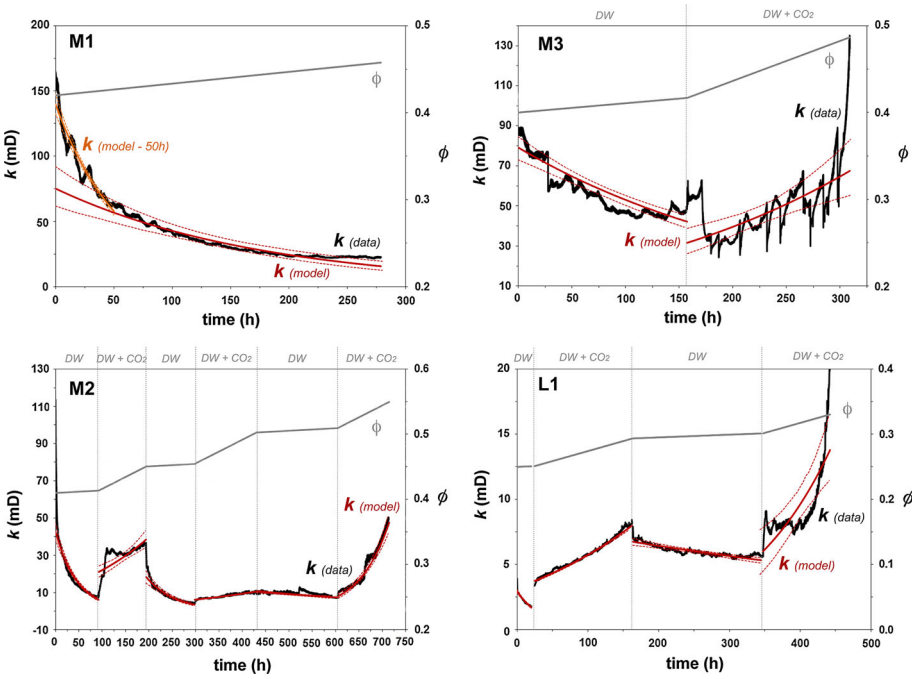


**Fig. 14** Temporal evolution of the permeability data [*solid black curves*, termed $k$ (*data*)] and the modeled values [*solid red curves*, termed $k$ (*model*)] for experiments M1, M2, M3 and L1. Modeled $k$ values obtained by fitting only data recorded during the first 50 h of experiment M1 [$k$ (*model 50 h*)] are also depicted (*solid orange curve*). *Dashed curves* denote 95 % confidence intervals. For all experiments, $\phi$ values determined through (3) are reported with *continuous gray curves*

**Table 2** Estimated values of $a_i^k = \ln A_i^k$ and $\alpha_i^k$ ($i$ = L1, M2, M3) obtained by (4) and of $b_i^k = \ln B_j^k$ and $\beta_j^k$ ($j$ = L1, M1, M2, M3) obtained by (5)

| | | | | |
|---|---|---|---|---|
| *DW* | | | | |
| M1 | $\hat{b}^1_{M1}$ | −30.23 | $\hat{\beta}^1_{M1}$ | $5.6 \times 10^{-3}$ |
| | | (−30.51; −29.96) | | $(3.8 \times 10^{-3}; 7.4 \times 10^{-3})$ |
| M1 first 50 h | $\hat{b}^1_{M1}$ | −29.61 | $\hat{\beta}^1_{M1}$ | $1.8 \times 10^{-2}$ |
| | | (−29.69; −29.54) | | $(1.5 \times 10^{-2}; 2.0 \times 10^{-2})$ |
| M2 | $\hat{b}^1_{M2}$ | −30.80 | $\hat{\beta}^1_{M2}$ | $2.1 \times 10^{-2}$ |
| | | (−30.95; −30.65) | | $(1.8 \times 10^{-2}; 2.3 \times 10^{-2})$ |
| | $\hat{b}^2_{M2}$ | −31.64 | $\hat{\beta}^2_{M2}$ | $1.6 \times 10^{-2}$ |
| | | (−31.91; −31.38) | | $(1.1 \times 10^{-2}; 2.0 \times 10^{-2})$ |
| | $\hat{b}^3_{M2}$ | −32.19 | $\hat{\beta}^3_{M2}$ | $2.1 \times 10^{-3}$ |
| | | (−32.30; −32.08) | | $(9.5 \times 10^{-4}; 3.2 \times 10^{-3})$ |
| M3 | $\hat{b}^1_{M3}$ | −30.18 | $\hat{\beta}^1_{M3}$ | $4.0 \times 10^{-3}$ |
| | | (−30.29; −30.08) | | $(2.9 \times 10^{-3}; 5.1 \times 10^{-3})$ |
| L1 | $\hat{b}^1_{L1}$ | −33.47 | $\hat{\beta}^1_{L1}$ | $2.7 \times 10^{-2}$ |
| | | (−33.56; −33.38) | | $(1.9 \times 10^{-2}; 3.4 \times 10^{-2})$ |
| | $\hat{b}^2_{L1}$ | −32.64 | $\hat{\beta}^2_{L1}$ | $1.3 \times 10^{-3}$ |
| | | (−32.70; −32.58) | | $(7.5 \times 10^{-4}; 1.9 \times 10^{-3})$ |
| *DW* + *CO*2 | | | | |
| M2 | $\hat{a}^1_{M2}$ | −25.28 | $\hat{\alpha}^1_{M2}$ | 7.05 |
| | | (−28.69; −21.87) | | (2.98; 11.12) |
| | $\hat{a}^2_{M2}$ | −28.50 | $\hat{\alpha}^2_{M2}$ | 5.37 |
| | | (−28.98; −28.03) | | (4.72; 6.02) |
| | $\hat{a}^3_{M2}$ | −16.49 | $\hat{\alpha}^3_{M2}$ | 23.72 |
| | | (−19.54; −13.43) | | (18.87; 28.56) |
| M3 | $\hat{a}^1_{M3}$ | −26.81 | $\hat{\alpha}^1_{M3}$ | 4.90 |
| | | (−29.43; −24.19) | | (1.63; 8.16) |
| L1 | $\hat{a}^1_{L1}$ | −26.50 | $\hat{\alpha}^1_{L1}$ | 4.87 |
| | | (−26.84; −26.16) | | (4.61; 5.14) |
| | $\hat{a}^2_{L1}$ | −21.95 | $\hat{\alpha}^2_{L1}$ | 9.01 |
| | | (−29.24; −14.65) | | (2.62; 15.40) |

Corresponding 95 % confidence limits are reported in parenthesis. Superscript $k$ represents the injection cycle number. The units for $A$, $\alpha$, $B$ and $\beta$ are, respectively, $m^2$, −, $m^2$ and $h^{-1}$

with DW+$CO_2$ injections, while parameters of (5) are estimated for the DW stages. Estimates $\hat{a}$, $\hat{b}$, $\hat{\alpha}$, and $\hat{\beta}$ of the parameters $a = \ln A$, $b = \ln B$, $\alpha$, and $\beta$ are listed in Table 2 together with the corresponding 95 % confidence limits for each phase of experiments M1, M2, M3 and L1.

The results depicted in Fig. 14 show a good agreement between the modeling results and the experimental data. This suggests that the simple interpretive model we propose can be employed to capture the key elements governing the general trend of the dynamics of $k$

observed at the core scale in terms of both the positive and anti-correlated $k - \phi$ regimes. One can note that the interpretation based on the best fit of the exponential model (5) for the long-lasting single-stage experiment M1 is not optimal. We argue that this is related to the issue discussed above and concerning the restriction of the reliability of our modeling approach to relatively low porosity changes. We further note that the latest part of the sharp permeability increase could not be captured when using (4) with a unique parameter pair $(\hat{A}, \hat{\alpha})$ for the whole period of time encompassing the last injection of DW + $CO_2$ . We suspect this sharp increase to be mainly linked to the finite-sized geometry of the experiment and thus to represent a boundary effect. The latter might be hampered in field-scale geological media, where one is typically interested in the behavior of regions that are located at a relatively large distance from the boundary.

As an additional term of comparison, Table 2 lists estimates $\hat{b}$ and $\hat{\beta}$ (together with the associated 95 % confidence limits) associated with M1 and obtained upon considering only the data recorded during the first 50 h of the experiment. The corresponding fit to M1 data is also depicted in Fig. 11 together with the associated 95 % confidence interval. As expected, the quality of the fit is markedly improved in comparison with that associated with the parameter estimates based on the full experimental dataset.

The model calibration results depicted in Fig. 15a for the DW + $CO_2$ cycles show that the $k - \phi$ trends are similar for all experiments. We note that the last DW + $CO_2$ injections (grouped as *inj3* in Fig. 15a) correspond to the breakout of the main flow paths. This results in a rapid increase of the sample permeability and in estimates $\hat{A}$ and $\hat{\alpha}$ which are markedly different from those related to the previous DW+$CO_2$ injection phases. Note that in Fig. 15a for experiment L1, where only two cycles have been performed, we report the values of the model parameters estimated during the second DW+$CO_2$ injection in the column termed *inj3* for ease of visual comparison. Trends of similar nature and associated with high estimates of exponent $\alpha$ were observed by Luquot and Gouze (2009). These authors estimated a power-law exponent $\alpha$ that increased from 0.79 to 4.79, the latter corresponding to settings where the main flow paths eventually reach the sample outlet. One should also consider that this situation is not completely relevant to in situ conditions because the large increase of permeability of the kind we observe for modest increase of porosity (which in turn implies large estimated values of $\alpha$) is due to the finite-size geometry of the system, i.e., it can be considered as an end-effect due to system finiteness. The values of $\alpha$ which we estimate and document here ($4.92 \leq \alpha \leq 6.44$) are similar to those found by Luquot et al. (2014) for diverse regimes of dissolution and two types of carbonate ($0.29 \leq \alpha \leq 7.01$).

Model calibration results depicted in Fig. 15b for the DW injection display enhanced variability across samples. The mechanism of particle accumulation during DW injection appears to have the same effect on permeability for samples M1 and M3 but not for samples M2 and L1, this being interpreted as the signature of distinctly different accumulation regimes.

Our data and conceptual interpretation suggest that the controlling role of the porous net-work morphology is much more pronounced on the anti-correlated $k - \phi$ trends documented during low reactive fluid injection than on the positive correlated $k - \phi$ trend observed during higher reactive fluid injection.

## 6 Conclusions

We investigate the dynamics of porosity ($\phi$) and permeability ($k$) in samples of two types of carbonate rocks during dissolution caused by injecting ($a$) deionized water (DW) and ($b$) DW enriched with $CO_2$ (DW + $CO_2$).

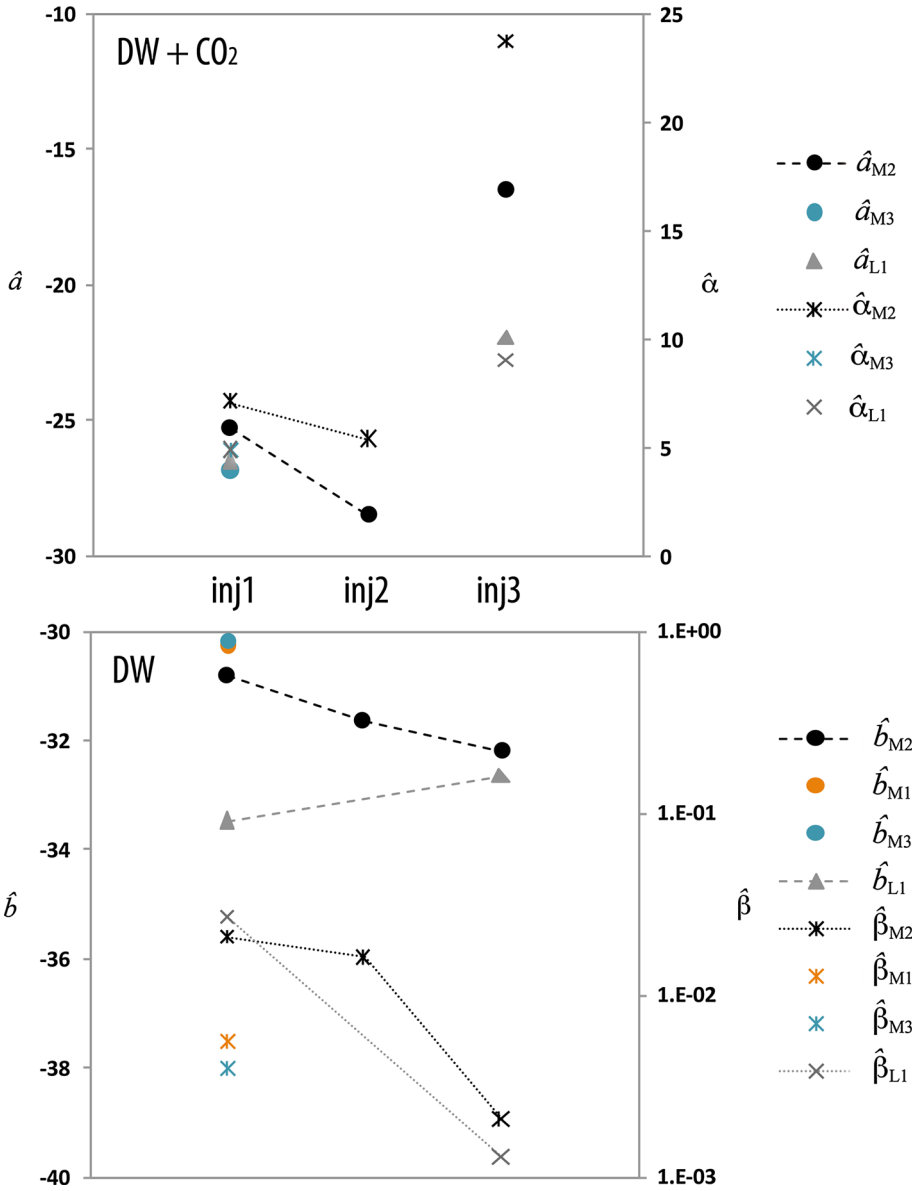


**Fig. 15** Estimated values of $a_i^k = \ln A_i^k$ and $\alpha_i^k$ ($i$ = L1, M2, M3) obtained by (4) and corresponding to the $DW + CO_2$ injection and of $b_j^k = \ln B_j^k$ and $\alpha_j^k$ ($j$ = L1, M1, M2, M3) obtained by (5) and corresponding to the DW injection. For experiment L1, the second cycle of $DW/DW + CO_2$ (i.e., last injections of $DW + CO_2$) is displayed in the *inj3* column for ease of visual comparison with experiment M2

Our work leads to the following major conclusions.

- The solid matrix of the two rock types results from the cementation of micrometer-sized (detritical) indurated grains with sparitic cement. As the reactive specific surface (i.e., the reactive surface per volume of material) of the cement is markedly higher than that of the

grains, we conjecture that the differential dissolution of the indurated grains and sparitic cement triggers the detachment of the grains that become suspended particles migrating in the pore space. This hypothesis is supported by detailed three-dimensional XRMT. The latter highlights the occurrence of particle accumulation at the pore-throat inlet when dissolution rate is low.

- Two $k - \phi$ trends are identified depending on the degree of undersaturation of the flowing solution. Permeability and porosity (a) are anti-correlated when the percolating fluid (DW) has a weak capacity of dissolution (i.e., low dissolution rate); and (b) exhibit a positive correlation when $CO_2$ is added to DW to significantly increase the dissolution potential of the fluid.
- We propose two simple phenomenological models to interpret the effect of the driving mechanisms on the observed $k - \phi$ correlations: (a) a power-law model suggested by Luquot and Gouze (2009) for highly reactive systems and (b) a two-parameter exponential model which we propose to employ when DW is flowing and the sample-scale permeability is controlled by the progressive clogging of the pore throats. The pro-posed models can properly interpret the occurrence of positive and negative $k - \phi$ cor-relations taking place when a rock sample is subject to cyclic DW + $CO_2$ and DW injections. Our conceptual picture and models are also consistent with the observation that the rate of decrease of permeability reduces for each subsequent flow of DW due to the increase of the effective pore-throat diameter triggered by the flow of DW + $CO_2$.

**Acknowledgments** We wish to thank Dr Elodie Boller (European Synchrotron Radiation Facility, Grenoble, France) for her precious help in the data acquisition and Dr Linda Luquot for the many constructive discussions concerning the experimental protocol setup. This study was supported by the EU-funded project PANACEA (EU-7thFP—ENERGY 282900).

## References

Appelo, C.A.J., Postma, D.: Geochemistry Groundwater and Pollution. A.A. Balkema Publishers, Rotterdam (1993)

Athy, L.F.: Density, porosity, and compaction of sedimentary rocks. AAPG Bull. **14**, 1–24 (1930)

Cohen, C., Ding, D., Quintard, M., Bazin, B.: From pore scale to wellbore scale: impact of geometry on wormhole growth in carbonate acidization. Chem. Eng. Sci. **63**, 3088–3099 (2008)

Fan, Y., Durlofsky, L.J., Tchelepi, H.A.: A fully-coupled flow-reactive-transport formulation based on element conservation, with application to $CO_2$ storage simulations. Adv. Water Resour. **42**, 47–61 (2012)

Garing, C.: Caractérisation géophysique et géochimique des interactions fluide-roche à l'interface eau douce-eau salée : cas des carbonates récifaux de Majorque. Ph.D. thesis, University of Montpellier 2, Montpellier, France (2011)

Garing, C., Luquot, L., Pezard, P.A., Gouze, P.: Electrical and flow properties of highly heterogeneous carbonate rocks. AAPG Bull. **98**(1), 49–66 (2014)

Golfier, F., Zarcone, C., Bazin, V., Lenormand, R., Lasseux, D., Quintard, M.: Ability of a Darcy-scale model to capture wormhole formation during the dissolution of a porous medium. J. Fluid Mech. **457**, 213–254 (2002)

Gouze, P., Luquot, L.: On the characterization of porosity–permeability relationships and reactive surface areas during heterogeneous dissolution induced by $CO_2$ injection in limestone reservoir. J. Contam. Hydrol. (2011). doi:10.1016/j.jconhyd.2010.07.004

Gouze, P., Noiriel, C., Bruderer, C., Loggia, D., Leprovost, R.: X-Ray tomography characterization of fracture surfaces during dissolution process. Geophys. Res. Lett. **30**(5), 1267–1270 (2003)

Gouze, P., Melean, Y., Le Borgne, T., Dentz, M., Carrera, J.: Non-Fickian dispersion in porous media explained by heterogeneous microscale matrix diffusion. Water Resour. Res. (2008). doi:10.1029/2007WR006690

Hao, Y., Smith, M.M., Sholokhova, Y., Carroll, S.A.: $CO_2$-induced dissolution of low permeability carbonates, part II: numerical modeling of experiments. Adv. Water Resour. **62**, 388–408 (2013)

Hebert, V.: Analyses multi-echelles de la structure d'un reservoir carbonate littoral: Exemple de la plateforme de Llucmajor (Majorque, Espagne). Ph.D. thesis, University of Montpellier 2, Montpellier, France (2011)
Hebert, V., Garing, C., Luquot, L., Gouze, P.: Multi-scale X-ray tomography analysis of carbonate porosity. In: Agar, S.M., Geiger, S. (eds.) Geological Society. Special Publications, London (2014). doi:10.1144/SP406.12
Kalia, N., Balakotaiah, V.: Modeling and analysis of wormhole formation in reactive dissolution of carbonate rocks. Chem. Eng. Sci. **62**(2007), 919–928 (2007)
Le Guen, Y., Hellmann, R., Collombet, M., Gratier, J.-P., Renard, F., Brosse, E.: Enhanced deformation of limestone and sandstone in the presence of high $P_{CO_2}$ fluids. J. Geophys. Res. B: Solid Earth (2007). doi:10.1029/2006JB004637
Luquot, L., Gouze, P.: Experimental determination of porosity and permeability changes induced by massive injection of $CO_2$ into carbonate reservoirs. Chem. Geol. (2009). doi:10.1016/j.chemgeo.2009.03.028
Luquot, L., Rodriguez, O., Gouze, P.: Experimental characterization of porosity structure and transport property changes in limestone undergoing different dissolution regimes. Transp. Porous Media (2014). doi:10.1007/s11242-013-0257-4
Luhmann, A.J., Kong, X.-Z., Tutolo, B.M., Garapati, N., Bagley, B.C., Saar, M.O., Seyfried Jr, W.E.: Experimental dissolution of dolomite by $CO_2$-charged brine at 100 °C and 150 bar: evolution of porosity, permeability, and reactive surface area. Chem. Geol. **380**, 145–160 (2014)
Mangane, P.O., Gouze, P., Luquot, L.: Permeability impairment of a limestone reservoir triggered by heterogeneous dissolution and particles migration during $CO_2$-rich injection. Geophys. Res. Lett. **40**(17), 4614–4619 (2013)
Meijster, A., Roerdink, J.B.T.M., Hesselink, W.H.: A general algorithm for computing distance transforms in linear time, Computational imaging and vision. Mathematical Morphology and Its Application to Image and Signal Processing **18**(8), 331–340 (2000)
Moore, C.H.: Carbonate reservoirs, porosity evolution and diagenesis in a sequence-stratigraphic frame-work. In: Developments in Sedimentology, vol. 55. pp. 1–444 (2001)
Noiriel, C., Bernard, D., Gouze, P., Thibault, X.: Hydraulic properties and microgeometry evolution accompanying limestone dissolution by acidic water. Oil Gas Sci. Technol. **60**, 177–192 (2005)
Noiriel, C., Luquot, L., Madé, B., Raimbault, L., Gouze, P., Van Der Lee, J.: Changes in reactive surface area during dissolution process: an experimental and modelling study. Chem. Geol. (2009). doi:10.1016/j.chemgeo.2009.01.032
Parkhurst, D.L., Appelo, C.A.J.: User's guide to PHREEQC (Version 2)—A computer program for speciation, batch-reaction, one-dimensional transport, and inverse geochemical calculations. US Geological Survey Water-Resources Investigations Report pp. 99–4259 (1999)
Pokrovsky, O.S., Golubev, S.V., Schott, J., Castillo, A.: Calcite, dolomite and magnesite dissolution kinetics in aqueous solutions at acid to circumneutral pH, 25 to 150 °C and 1 to 55 atm $P_{CO_2}$: new constraints on $CO_2$sequestration in sedimentary basins. Chem. Geol. **265**, 20–32 (2009)
Qajar, J., Francois, N., Arns, C.H.: Microtomographic characterization of dissolution-induced local porosity changes including fines migration in carbonate rock. SPE J. **18**(3), 545–562 (2013)
Rutqvist, J., Stephansson, O.: The role of hydromechanical coupling in fractured rock engineering. Hydrol. J. **11**, 7–40 (2003)
Saaltink, M., Vilarrasa, V., de Gaspari, F., Silva, O., Carrera, J., Rötting, T.S.: A method for incorporating equilibrium chemicals reactions into multiphase flow models for $CO_2$ storage. Adv. Water Resour. **62**, 431–441 (2013)
Sahimi, M.: Applications of Percolation Theory. CRC Press, Taylor & Francis, London (1994)
Schneider, F., Potdevin, J.L., Wolf, S., Faille, I.: Mechanical and chemical compaction model for sedimentary basin simulators. Tectonophysics **263**, 307–313 (1996)
Siena, M., Guadagnini, A., Riva, M., Bijeljic, B., Pereira Nunes, J.P., Blunt, M.J.: Statistical scaling of pore-scale Lagrangian velocities in natural porous media. Phys. Rev. E. **90**, 023013 (2014)
Smith, M.M., Sholokhova, Y., Hao, Y., Carroll, S.A.: $CO_2$-induced dissolution of low permeability carbonates, part I: characterization and experiments. Adv. Water Resour. **62**, 370–387 (2013)
Tutolo, B.M., Luhmann, A.J., Kong, X.-Z., Saar, M.O., Seyfried Jr, W.E.: Experimental observation of permeability changes in dolomite at $CO_2$ sequestration conditions. Environ. Sci. Technol. (2014). doi:10.1021/es4036946
Wang, X., Alvarado, V., Swoboda-Colberg, N., Kaszuba, J.P.: Reactivity of dolomite in water-saturated supercritical carbon dioxide: significance for carbon capture and storage and for enhanced oil and gas recovery. Energy Convers. Manag. **65**, 564–573 (2013)